

# Lithium concentration and atomic chain bridging induced strength–ductility synergy in amorphous lithiated sulfur cathodes

Yuan Gao <sup>a</sup>, Siyi Huang <sup>a</sup>, Xiaoyan Li <sup>b</sup>, Yuli Chen <sup>a</sup>, Bin Ding <sup>a,\*</sup>

<sup>a</sup> National Key Laboratory of Strength and Structural Integrity, Institute of Solid Mechanics, School of Aeronautic Science and Engineering, Beihang University, Beijing 100191, China

<sup>b</sup> Center for Advanced Mechanics and Materials, Applied Mechanics Laboratory, Department of Engineering Mechanics, Tsinghua University, Beijing 100084, China



## ARTICLE INFO

### Keywords:

Lithium ion battery  
Sulfur cathodes  
Brittle to ductile transition  
Atomic chain bridging  
Strength–ductility synergy

## ABSTRACT

As an eminent candidate for next-generation cathode materials, sulfur undergoes severe volume changes during electrochemical cycling, resulting in material fractures and performance degradation. Although the electrochemical characteristics of lithiated sulfur have been rigorously studied, their mechanical properties, particularly fracture mechanisms, remain insufficiently understood. To address this gap, we conducted comprehensive atomistic simulations to investigate the fracture behavior of amorphous lithiated sulfur ( $\text{a-Li}_x\text{S}$ ). Our findings reveal that as lithium concentration increases, the fracture mechanism transits from brittle governed by nanoscale cavitation instability to ductile dominated by plastic shear bands launched at the crack tip. This transition is contingent upon local hydrostatic stress exceeding the cavitation strength, elucidated through atomic-level bonding dynamics including rupture, reformation and rotation. At low lithium concentrations, atomic chain bridging posterior to the crack tip is simultaneously identified to enhance crack resistance. The lithiation-induced fracture toughness enhancement is further quantified via domain  $J$ -integral analysis. Notably, a unique strength–ductility synergy is identified for  $\text{a-Li}_x\text{S}$ , attributed to cooperation between lithiation induced heterogeneous bonding environments and atomic chain bridging. This study provides valuable atomic-scale insights into the fracture mechanisms of sulfur cathodes, thereby informing the design of high-energy and durable electrode materials for future applications.

## 1. Introduction

In recent years, industries such as portable electronic devices, electric vehicles and robots have set increasingly stringent requirements for the energy storage performance of batteries (Kim et al., 2019). Lithium-ion batteries, known for their high energy density and long cycle life, have become widely utilized. Sulfur, which possesses one of the highest energy densities as a cathode material for lithium-ion batteries with a theoretical specific capacity reaching 1672 mAh/g, offers more than ten times the specific capacity of the conventional  $\text{LiCoO}_2$  cathode (Manthiram et al., 2014). Moreover, sulfur is abundant in nature, non-toxic, environmentally friendly, emerging as a promising electrode material for the next-generation lithium-ion batteries (Shao et al., 2023). Nevertheless, challenges like the high reactivity of lithium, notable structural and volume changes in the cathode, and the dissolution

\* Corresponding author.

E-mail address: [bin\\_ding@buaa.edu.cn](mailto:bin_ding@buaa.edu.cn) (B. Ding).

of intermediate polysulfides into the electrolytes lead to rapid capacity degradation during electrochemical cycles, impeding the broader commercialization of lithium-sulfur batteries (Wang et al., 2022; Yang et al., 2020).

Previous studies have demonstrated that, at macroscale, electrode materials undergo large volume expansions and contractions during charge-discharge cycles, which often result in electrode fractures and performance degradation (de Vasconcelos et al., 2022; Ding et al., 2017; Li et al., 2019; Liu et al., 2017; Sandu et al., 2014; Singh and Pal, 2020; Tancogne-Dejean et al., 2021; Zhu et al., 2019). Nanoscale electrodes are more resilient to this challenge owing to their ample space, allowing accommodation for volume changes (Chan et al., 2008). To prolong the cycle life of electrodes, several strategies have been proposed, including the use of carbon nanospheres, TiO<sub>2</sub> nanospheres and carbon nanotubes to externally regulate and mitigate electrode volume variations, as well as employing self-healing gels to repair cracked or damaged electrodes (Bai et al., 2023; Chen et al., 2016; Chen et al., 2022a; Liu et al., 2021). However, cathode degradation resulting from mechanical deformations still substantially impairs performance. More notably, unlike silicon with covalent bonds, sulfur is primarily connected by covalent S–S bonds within S rings or chains, along with weak van der Waals interactions between these rings or chains. These distinctions in atomic structure highlight the challenge of directly applying conclusions derived from studies on silicon anodes to sulfur cathodes (Ding et al., 2015; Khosronejad and Curtin, 2017; Wang et al., 2015). A systematic investigation into the fracture behaviors of lithiated sulfur becomes imperative.

Scanning electron microscopy (SEM) observations of the lithiation and delithiation processes in sulfur electrodes indicate that lithiated sulfur predominantly exists in amorphous state (Zhang et al., 2019). Given the need for fundamental understanding of the whole fracture processes at smaller scales is beyond the capabilities of current experiments, Islam et al. developed ReaxFF potential apt for the Li–S system and then conducted several ReaxFF-based molecular dynamics (MD) simulations on a-Li<sub>x</sub>S for validation (Islam et al., 2015; Senftle et al., 2016). Their findings suggest that at lithium concentration  $x = 0.8$ , brittle fracture arises under uniaxial tension. Subsequently, Wang et al. examined a-Li<sub>x</sub>S with  $x = 1.6$  by loading on a finite-width crack and identified a ductile fracture mode characterized by shear band driven ductile fracture (Wang et al., 2017). It can be conjectured that as lithium concentration increases, the fracture mode for a-Li<sub>x</sub>S transitions from brittle to ductile. However, the underlying mechanisms for this transition remain unknown. Consequently, the fracture behaviors of a-Li<sub>x</sub>S are not fully understood, primarily due to the limited studies on lithium concentration variations. A thorough and systematic investigation is crucial.

The strength-ductility trade-off has been a persistent challenge in the fields of engineering and materials science. Presently, there are two predominant approaches for the concurrent enhancement of both strength and ductility. The first involves microstructure control, such as the introduction of grain boundaries (GB) and phase boundaries to impede dislocation propagation, grain size refinement to activate non-basal slip systems due to GB compatibility stress, and the use of heterostructure with mutual constraints between hard and soft domains to accumulate geometrically necessary dislocations (GND) (Chen et al., 2022b; Hasan et al., 2019; Kim et al., 2022; Luo et al., 2020b; Xiang and Guo, 2022). These technologies, however, often necessitate intricate preparation processes. The second approach emphasizes compositional control, encompassing strategies such as elemental doping and optimizing short-range ordering to improve the strength and ductility of materials like high-entropy alloys (Chen et al., 2021; He et al., 2021). Yet, determining the optimal composition frequently requires extensive experimental and computational investigation. Currently, there remains a dearth of simple and direct methods to augment strength and toughness at the same time.

In this study, through extensive large-scale atomistic simulations and comprehensive theoretical analyses, we have identified that electrochemical lithiation can simultaneously enhance strength and ductility of amorphous lithiated sulfur cathodes in lithium-ion batteries, which diverges from the conventional strength-ductility trade-off. First, we explore the influence of lithium concentration on the fracture behavior of a-Li<sub>x</sub>S with a comprehensive lithium concentration range from 0 to 1.6. The fracture behavior of a-Li<sub>x</sub>S is governed by both cavitation nucleation in front of the crack tip and atomic chains bridging behind the crack tip. The nucleation of cavitation at the crack tip dictates the transition from brittle to ductile fracture in a-Li<sub>x</sub>S, which is attributed to the heterogeneous bonding dynamics resulting from lithiation. Crack resistance at low lithium concentration is enhanced by the atomic chain bridging behind the crack tip, while transferred to suppression cavitation nucleation and crack blunting at high lithium concentration. We conduct domain J-integral calculations to ascertain  $J_{IC}$  at various lithium concentrations, thereby quantifying a monotonous toughening effect. The synergy between strength and ductility is further underscored by lithiation induced heterogeneous bonding dynamics and atomic chain bridging.

## 2. Methods

A series of MD simulations were conducted to generate and load various a-Li<sub>x</sub>S samples using the ReaxFF potential.

$$E = E_{\text{bond}} + E_{\text{over}} + E_{\text{under}} + E_{\text{lp}} + E_{\text{val}} + E_{\text{tor}} + E_{\text{vdWaals}} + E_{\text{Coulomb}} \quad (1)$$

where potential energy contributions include bond, over-coordination penalty and under-coordination stability, lone pair, valence, and torsion, non-bonded interactions van der Waals, and Coulomb energies, respectively (Islam et al., 2015; Senftle et al., 2016). The ReaxFF potential is capable of utilizing bond orders to determine bonded interactions, enabling accurate predictions for mechanical properties of both crystalline and amorphous LiS alloys. The measurements of bond lengths and energies are in good agreement with both experimental data and first principle calculations. This alignment substantiates the reliability of our MD models and the subsequent calculation of fracture energy using atomic information from MD (Islam et al., 2015; Luo et al., 2020a). Melting-and-quenching processes, consistent with our previous works, were employed to generate a-Li<sub>x</sub>S sample with lithium concentrations  $x$  set at 0, 0.4, 0.8, 1.2, and 1.6. Beginning with  $\alpha$ -sulfur, with lithium atoms randomly inserted at specified ratios, the system was heated to 1600 K and relaxed for 125 ps to attain an equilibrium state. Subsequently, the quenching process involved

cooling the sample from 1600 K to 1 K in 160 ps, with a quenching rate of 10 K/ps. Throughout the melting-and-quenching processes, NPT ensembles with zero pressure were maintained and periodic boundary conditions (PBC) were imposed in all three directions. The generated a-Li<sub>x</sub>S samples had dimensions of approximately 45 × 35 × 2 nm<sup>3</sup>. Following the melting-and-quenching process, an additional relaxation at 1 K was carried out for 100 ps to reach the energy minimization state, producing the a-Li<sub>x</sub>S samples ready for subsequent Mode-I loading simulations.

Mode-I loading simulations were then performed on each sample. A sharp edge crack with a length of 17 nm was introduced by excluding atomic interaction across the crack surfaces. The atomic layers at the upper and lower edges of the sample, each with a thickness of 0.5 nm, were rigidly fixed and subjected to zero force and angular velocity. The two rigid atomic layers along the crack direction were then moved with a constant velocity, and linear velocity gradients were applied to all internal atoms based on their coordinates (Ghaemi et al., 2022; Pogorelko and Mayer, 2023; Xie et al., 2023; Zeng et al., 2021). During Mode-I loading, a constant strain rate of  $5 \times 10^8$  s<sup>-1</sup> was maintained. Note that while many mechanical properties of materials are sensitive to the loading rate, the high loading rates typically used in MD do not usually qualitatively alter the physical nature of deformation (Li and Gao, 2015). The system's temperature was kept at 1 K by the Berendsen thermostat throughout the loading process to minimize the influence of thermal fluctuations on the results. Employing this temperature enables a focused examination of the underlying mechanism, isolating it from the confounding effects of thermal fluctuations on fracture phenomena. Periodic boundary condition was imposed in the thickness direction, while shrink-wrap boundary conditions were applied to the other directions. The integration time step was set at 0.25 fs. All simulations were performed by LAMMPS (Plimpton, 1995).

The stress is calculated by the virial theorem:

$$\sigma_{ij} = \frac{1}{\Omega} \sum_{\alpha} \left[ \frac{1}{2} \sum_{\beta=1}^N (x_i^{\alpha} - x_i^{\beta}) F_j^{\alpha\beta} - m^{\alpha} v_i^{\alpha} v_j^{\alpha} \right] \quad (2)$$

where  $i$  and  $j$  denote the directions  $x$ ,  $y$ ,  $z$ ,  $\Omega$  is the total volume,  $\beta$  takes values 1 to  $N$  neighbors of atom  $\alpha$ ,  $x_i^{\alpha}$  is the position of atom  $\alpha$  along direction  $i$ ,  $F_j^{\alpha\beta}$  represents the interaction force along direction  $j$  on atom  $\alpha$  due to atom  $\beta$ ,  $m^{\alpha}$  is the mass of atom  $\alpha$ ,  $v^{\alpha}$  is the thermal excitation velocity of atom  $\alpha$ . The first term of the equation is the virial contribution due to intra and intermolecular interactions; the second term is the kinetic energy contribution, which can be ignored when the temperature approximates 0 K.

### 3. Results and discussions

#### 3.1. Brittle to ductile transition in a-Li<sub>x</sub>S as lithium concentration increases

**Fig. 1a–e** present a series of snapshots of crack propagation in a-Li<sub>x</sub>S with different lithium concentration  $x$  during loading. Atoms are colored according to the local von Mises strain. During crack propagation, our simulations unveil two distinct fracture behaviors. For samples with lower lithium concentrations ( $x \leq 1.2$ ) as shown in **Fig. 1a–d**, nanosized voids spontaneously nucleate ahead of the crack. These voids gradually grow and eventually coalesce with the main crack, leading to swift crack propagation and exemplifying brittle fracture behavior. This behavior of nanosized void nucleation, growth, and coalescence was also identified in FeP metallic glasses, suggesting it as a representative mechanism responsible for brittle fracture in amorphous materials (Murali et al., 2011). This presence of nanosized voids has been reported in subsequent studies through simulations, in brittle materials such as low-lithiated amorphous lithiated silicon, amorphous carbon, Mg- and La-based metallic glasses, molten and solid Al (Ding et al., 2015; Khosrownejad and Curtin, 2017; Khosrownejad et al., 2021; Mayer and Mayer, 2019). Furthermore, cavitation nucleation phenomena were also experimentally validated in metallic glasses by atomic force microscopy (AFM) (Shen et al., 2021). In contrast, for samples with higher lithium concentrations ( $x > 1.2$ ) as shown in **Fig. 1e**, no cavitation exhibits. Instead, extensive shear bands launch at the crack tip.

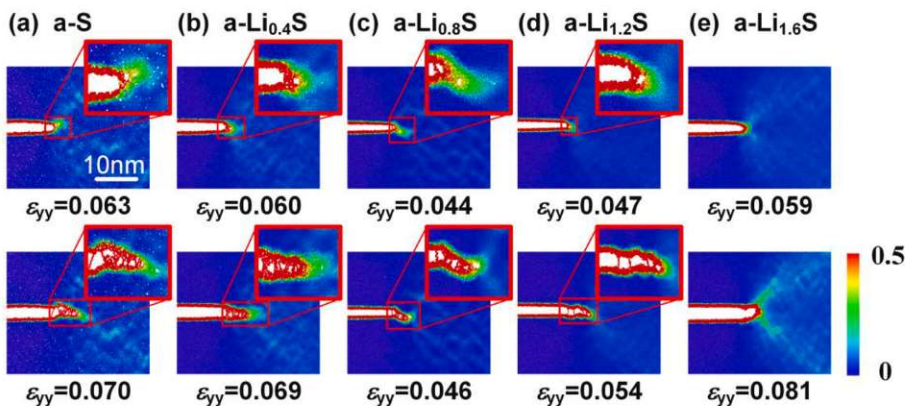


**Fig. 1.** Snapshots of crack propagation of a-Li<sub>x</sub>S at various applied strains  $\varepsilon_{yy}$ . Panels (a–e) represent the fracture behavior of (a) a-S, (b) a-Li<sub>0.4</sub>S, (c) a-Li<sub>0.8</sub>S, (d) a-Li<sub>1.2</sub>S, and (e) a-Li<sub>1.6</sub>S. The strain is calculated as  $\delta h/h$ , where  $h$  denotes the height of the sample. Atoms are colored according to local values of their von Mises strain. Insets in (a–d) highlight cavitation nucleation ahead of the crack tip (top) and atomic chain bridging trailing the crack tip (bottom). The scale bar of 10 nm is presented in (a) and remains consistent throughout (a–e).

As the loading continues, this sample undergoes significant plastic deformation, leading to expansive plastic zones near the crack tip. Our previous study emphasized this phenomenon was particularly prominent in samples with infinite large lithium concentration as amorphous lithium (Ding et al., 2015). These observations suggest that lithiated sulfur embraces a ductile fracture mode at higher lithium concentrations. Collectively, the determination of the fracture mechanism (brittle or ductile) in a-Li<sub>x</sub>S hinges on whether cavitation nucleation occurs. We discern a transition from brittle to ductile fracture in a-Li<sub>x</sub>S as lithium concentration increases. The underlying mechanism shifts from the nucleation, growth and coalescence of nanoscale voids to the launch of shear bands.

More notably, atomic chains are observed behind the crack tip. As the crack propagates, these atomic chains form connections with both crack surfaces, serving as atomic bridges. These bridges hinder the crack advancement and facilitate increased energy dissipation. The stress-strain curves during loading as depicted in Fig. S1 demonstrate that at lower lithium concentrations ( $x \leq 0.4$ ), the failure strain corresponding to the peak stress is larger, suggesting a predominant presence of atomic chains. While as lithium concentration increases ( $x > 0.4$ ), the atomic chains become less prevalent, resulting in a decrease in the failure strain associated with the peak stress. Movies of crack propagations in a-Li<sub>x</sub>S with different lithium concentration  $x$  are provided in the Supplementary Information.

To elucidate the correlation between cavitation nucleation and lithium concentration, we examined the critical hydrostatic stress required for spontaneous void nucleation in a-Li<sub>x</sub>S at different lithium concentrations. A series of hydrostatic tensile tests were performed on cubic a-Li<sub>x</sub>S samples with varying lithium concentrations. These tests aimed to establish the relationship between hydrostatic stress and volume strain, with the peak stress recorded as the cavitation stress  $\sigma_c$ . To eliminate size effects, we adopted five sample sizes, ranging from 0.8 nm to 8 nm for each specific lithium concentration. For each designated size, seven distinct cubic samples were randomly sliced from a 10 nm-sized cube. The variation of the cavitation stress with lithium concentration and sample size is depicted in Fig. S2. The findings underscore a substantial association between cavitation stress and sample size. As the sample size increases, the cavitation stress gradually saturates at a steady value. Notably, an evident dependency of cavitation stress on lithium concentration was observed, increasing with higher lithium concentrations.

Fig. 2 shows the variations of local hydrostatic stress  $\sigma_h$  with the distance ahead of the crack tip in a-Li<sub>x</sub>S samples at the onset of crack propagation. The local hydrostatic stresses are calculated through spatial averaging over a 1 nm square area on both the upper and lower sides of the crack epitaxial lines, consistent with the methodologies employed in reference (Ding et al., 2015; Murali et al., 2011). Upon integrating the upper and lower bounds of the cavitation stress from Fig. S2 into Fig. 2, it becomes evident at lower lithium concentrations ( $x \leq 1.2$ ), the peak local hydrostatic stress at the crack tip lies within the range of the cavitation stress, successfully predicting the nanoscale cavitation nucleation at the crack tip. Conversely, at higher lithium concentrations ( $x > 1.2$ ), the maximum local hydrostatic stress at the crack tip remains below the lower bound of the cavitation stress, inhibiting the cavitation

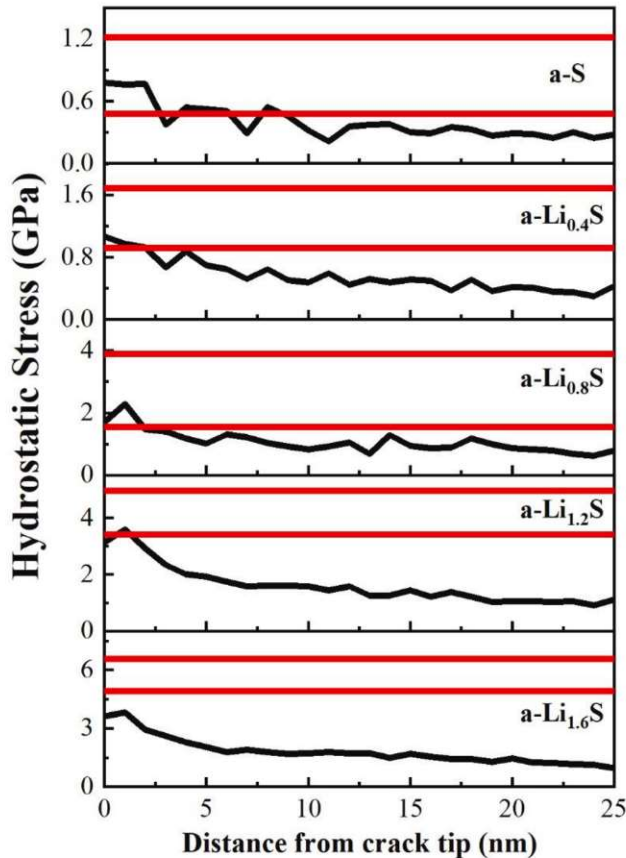


**Fig. 2.** Variation in local hydrostatic stress of a-Li<sub>x</sub>S as a function of distance from the crack tip at the onset of crack propagation. The red lines denote the range of cavitation stresses, encompassing the maximum and minimum values derived from atomic scale fluctuations from Fig. S2.

nucleation, and thereby crack propagation is governed by shear bands.

### 3.2. Atomic scale bonding dynamics at the crack tip

To further study the atomic scale deformation behaviors accompanying the transition in fracture mechanisms, we analyzed atomic bonding dynamics at the crack tip for each sample at the onset of crack propagation. As the ReaxFF potential employs the concept of bond order to govern bonding interactions, it enables the breaking and formation of chemical bonds (Senftle et al., 2016; Wang et al., 2015). At lower lithium concentrations ( $x \leq 0.4$ , Fig. 3a-b), local deformations near the crack tip are primarily accommodated by the elongation and rupture of S–S bonds. Due to the higher proportion of strong covalent S–S bonds, changes in atomic chemical bonding largely occur in a discrete and abrupt manner, lacking bond reformation. Conversely, at large lithium concentrations ( $x > 0.4$ , Fig. 3c-e), local tensile deformations are accommodated through the breaking, rotating, stretching, and frequent recombination of Li–S and Li–Li bonds. An increased number of Li atoms engage in bond switching activities during loading. The statistics of diverse atomic bond behaviors are represented in Fig. S3, offering a quantitative depiction of the influence of lithium concentration. These findings illuminate an atomic-scale rational for the brittle-to-ductile transition in a-Li<sub>x</sub>S. Increasing lithium concentrations breaks S ring-s/chains and augment ionic S–Li as well as metallic Li–Li bonds, thereby altering atomic bonding behaviors during deformation and fracture events. This provides novel insights into the atomic-scale fracture mechanisms. Radial distribution functions (RDFs) of S–S, S–Li and Li–Li in a-Li<sub>x</sub>S are delineated in Fig. S4 to further corroborate structural attributes.

### 3.3. Atomic chain bridging enhanced crack resistance at low lithium concentrations

In addition to the cavitation phenomenon at the crack tip, we also noted atomic chains behind the crack tip, reminiscent of crack bridging often seen in fiber-reinforced composites and twinned materials (Monismith et al., 2022; Zeng et al., 2021). Fig. 4a shows the principle of atomic chains toughening, as the crack extends further, these atomic chains connect with the two fracture surfaces, acting as bridges that impede crack propagation and result in additional energy dissipation. These atomic chains are mainly long-chain lithium polysulfides, which is consistent with the experimental findings on the shuttle effect of polysulfides (Lee et al., 2022; Manthiram et al., 2013). To verify the feasibility of atomic chain structures, we have provided DFT verifications on their structural stabilities in Fig. S5. In order to further analyze the influence of atomic chains on crack propagation, we plotted the variation of the crack tip extension distance  $\Delta a$  with strain, as shown in Fig. 4b. At lower lithium concentrations ( $x \leq 0.4$ ), crack starts to propagate at a relatively low loading strain, but the presence of atomic chains acts as a hindrance, delaying rapid crack propagation. This is particularly notable in non-lithiated sulfur, where a long plateau segment exists after crack initiation. As lithium concentration increases ( $x > 0.4$ ), the number of atomic chains decreases, and the strengthening effect introduced by the lithiation process begins to dominate. Consequently, both the critical strain for crack initiation and for rapid propagation increase. This phenomenon is consistent with the stress-strain curves of a-Li<sub>x</sub>S samples with an edge crack as shown in Fig. S1, where lower lithium concentrations exhibit larger failure strains corresponding to the peak stress.

To investigate how the enhanced bonding dynamics affects atomic chains, two isolated systems with single atom pair were constructed, including two sulfur atoms and one sulfur atom with one lithium atom, respectively, as schematically illustrated by the insets in Fig. 4c. In these systems, one atom is fixed while the other is moved away. The interaction energy between the two atoms as a function of distance was measured by ReaxFF used in this study and plotted in Fig. 4c. The most stable interatomic distances for S–S

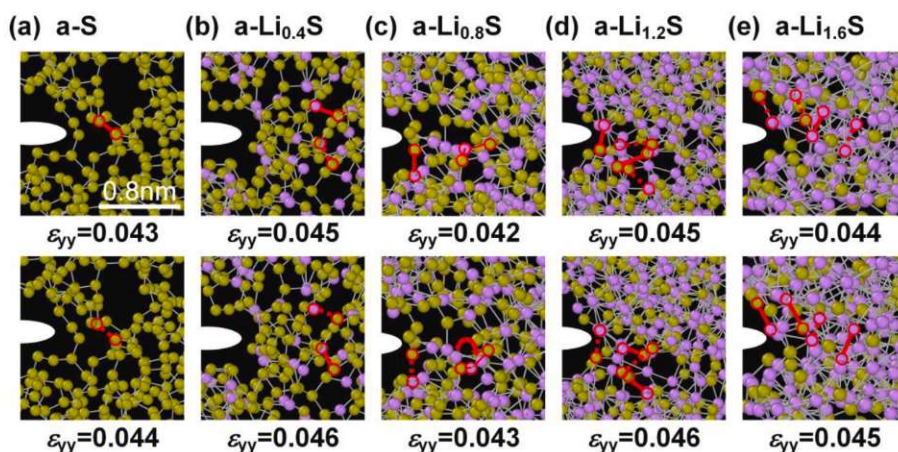


**Fig. 3.** Zoom-in snapshots in proximity to the crack tip of a-Li<sub>x</sub>S at the onset of crack propagation. (a-e) The atomic deformation behavior of (a) a-S, (b) a-Li<sub>0.4</sub>S, (c) a-Li<sub>0.8</sub>S, (d) a-Li<sub>1.2</sub>S, (e) a-Li<sub>1.6</sub>S. These snapshots highlight the characteristic deformation behavior, including bond breaking (transitioning from solid to dashed lines), bond reformation (transitioning from dashed to solid lines), and bond rotation (evidenced by the angle change between two red lines). At lower lithiation concentrations, the change of chemical bonds is mainly discrete breakings, but with the increase of lithiation concentrations, the behavior of chemical bonds is mainly reformation. Sulfur and lithium atoms are colored by yellow and purple, respectively, in (a-e). The scale bar of 0.8 nm is presented in (a) and remains consistent throughout (a-e).

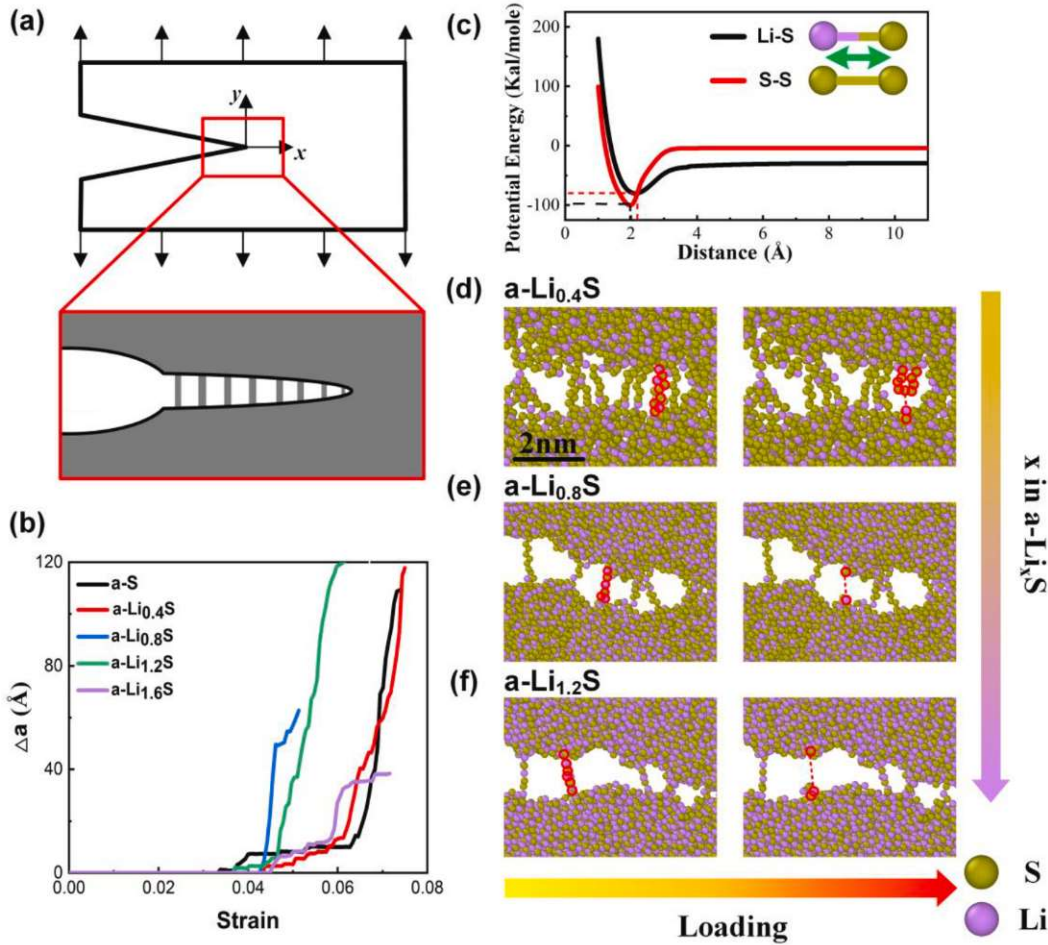


**Fig. 4.** Analysis of the toughening mechanism facilitated by the atomic chain located posterior to the crack tip. (a) Schematic of a crack with atomic bridging in a-LixS. (b) Relationship between crack propagation distance and strain of a-LixS with different lithium concentrations. (c) Energy variation in relation to the distance for both S-S and Li-S atom pairs. The dashed line denotes the potential energy and distance at the energy's nadir. (d-f) Fracture processes of the atomic chain during loading with different lithium concentrations in a-LixS. Atoms highlighted by the red circle indicate the impending chain breakage, while the adjacent dotted line signifies the precise breakage location. The scale bar of 2 nm is presented in (d) and remains consistent throughout (d-f).

and Li-S were determined to be  $r_0 = 2.03 \text{ \AA}$  and  $2.14 \text{ \AA}$ , respectively, which correspond to the equilibrated bond lengths of S-S and Li-S ( $2.07 \text{ \AA}$  from the pair distribution function experiments and  $2.20 \text{ \AA}$  from the MD simulations, respectively) (Islam et al., 2015; Luo et al., 2020a). These distances are associated with minimum energies of  $E_0 = -2.17 \text{ eV}$  for S-S bonds and  $-1.74 \text{ eV}$  for Li-S bonds. The results indicate that the minimum potential energy of Li-S bond is higher than that of S-S bond, implying that the strength of the Li-S bond is weaker than that of the S-S bond. By observing morphologies based on atom types and monitoring the behavior of atomic chains frame by frame, it was noted that with the progression of loading, atomic chains experience breaking. The majority of breaks occur between S and Li atoms, as shown in Fig. 4d-f, which is consistent with the simulated results of atomic bond strengths. It is noteworthy that atomic chains are predominantly composed of S-S bonds and a minority of Li-S bonds, with the absence of Li-Li bonds. This stable configuration results from the inherent structure of unlithiated S rings/chains.

### 3.4. Strength-ductility synergy in a-LixS as lithium concentration increases

In order to quantify the enhanced toughening effect of the lithiation process on the fracture toughness of a-LixS compounds, we computed the fracture energy. Considering the severe nonlinear deformation behavior of a-LixS samples especially at higher lithiation concentrations, we employ the domain  $J$ -integral method at the atomic scale to accurately calculate the fracture energy as a measure of ductility for different lithium concentrations (Jones and Zimmerman, 2010; Rice, 1968; Xie et al., 2023). The  $J$ -integral forms involves a closed contour integral of strain energy density and the work done by tractions on the contour is as follows:

$$J = \int_{\Gamma} \left( w n_i - \sigma_{ij} n_j \frac{\partial u_i}{\partial x_1} \right) d\Gamma \quad (3)$$

where the contour  $\Gamma$  starts at any point on the lower crack face and ends at any point on the upper crack face,  $w$  is the strain energy

density,  $\sigma_{ij}$  and  $u_i$  denote components of stress and displacement, respectively, 1 is the direction parallel to the crack, and  $n_j$  is the unit vector outward normal to the contour  $\Gamma$ . Given the inherent discrete character of atomistic models in molecular dynamics simulations, contour integration cannot be applied directly. Therefore, this study utilized the atomic-scale equivalent domain  $J$ -integral approach. This method encompasses the ring-shaped domain around the crack tip with a closed contour. This contour consists of an inner circle  $\Gamma_0$  with radius  $r_0$ , an outer circle  $\Gamma_1$  with radius  $r_1$  and two crack faces. Subsequently, the domain integral formula can be derived as

$$J = \int_A \left[ w \frac{dg}{dx_1} - \sigma_{kj} \frac{dg}{dx_k} \frac{\partial u_j}{\partial x_1} \right] dA \quad (4)$$

where  $g$  is the introduced auxiliary function taken as  $g = (r - r_0)/(r_1 - r_0)$ . We used the regional average method to transform atomic scale discrete values into continuum. Further detailed deviation process is elaborated in the Supplementary Information.

**Fig. 5a** shows the calculated domain  $J$ -integral values  $J_{IC}$  from eight integral domains with different inner and outer radius, as a function of the lithium concentration  $x$  in a-Li<sub>x</sub>S at the onset of crack propagation. All calculated  $J$ -integral values for each integral domain are provided in Table S1. Our computational results indicate that the fracture toughness  $J_{IC}$  of a-Li<sub>x</sub>S varies between 0.445 and 3.194 J/m<sup>2</sup> for different lithiation concentrations. Among these, the fracture toughness value for a-S is 0.445 J/m<sup>2</sup>, which is slightly larger than twice of the c-S surface energy of 0.188 J/m<sup>2</sup> calculated by density functional theory (DFT) calculations, evidenced the correctness of our calculations (Holeki Chandrappa et al., 2022). With an increase in lithium concentration, the  $J$ -integral values exhibit a monotonous upward trend. When the lithium concentration is relatively low ( $x \leq 1.2$ ), the calculated  $J$ -integral values show a rapid growth with increasing lithium concentration, indicating a significant toughening effect introduced by lithiation induced bonding dynamics as well as atomic chain bridging. Conversely, at higher lithium concentrations ( $x > 1.2$ ), the growth rate of  $J$ -integral values slows down as the concentration of lithium within the sample becomes higher. At this point, the additional enhancement from further lithiation becomes less pronounced.

Yield strengths are also collected by uniaxial tensile loadings on a-Li<sub>x</sub>S samples, with stress-strain curves for the strain rates of  $5 \times 10^8$  s<sup>-1</sup> available in Fig. S6, Supplementary Information. We observe that during initial lithiation, the strength increases rapidly, but when the lithium concentration is higher ( $x > 1.2$ ), the strengthening is not substantial. This may be due to initial lithium insertion breaks S–S rings and forms Li–S bonds, leading to the increase in strength. While lithium content is higher, the formation of Li–Li bonds has a lesser contribution to the strength growth.

More notably, it is observed that the increase in fracture toughness  $J_{IC}$  exhibits a similar trend to the increase in strength, suggesting that the lithiation process concurrently enhances both toughness and strength. This strength-ductility synergy in a-Li<sub>x</sub>S is surprisingly contrary to the strength-ductility tradeoff in a-Li<sub>x</sub>Si, as shown in **Fig. 5b**. With the increase of lithium concentration, the toughness of a-Li<sub>x</sub>Si first slightly decreases and then increases, the strength of a-Li<sub>x</sub>Si decreases rapidly at first, and then tend to be stable (Khosrownejad and Curtin, 2017; Sethuraman et al., 2010; Wang and Chew, 2016; Wang et al., 2015; Yang and Qu, 2019). The toughening effect is due to that lithiation augments toughness and ductility of a-Li<sub>x</sub>Si, same as that of a-Li<sub>x</sub>S. The softening effect is due to the strong covalent Si–Si bonds breaking and being replaced by weaker Li–Si and Li–Li bonds. Consequently, the insertion of lithium into diamond-structured Si leads to an increase in toughness but a decrease in strength. In contrast, lithium insertion into ring-structured S results in enhancements in both toughness and strength. This distinction underscores the varying mechanical responses elicited by

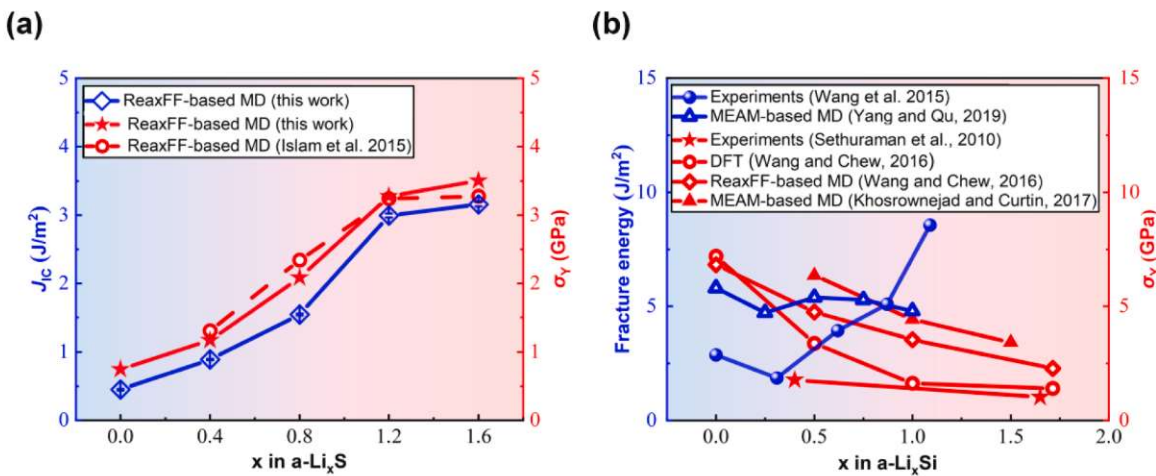


**Fig. 5.** The fracture energy and strength as a function of Li concentration  $x$  for (a) a-Li<sub>x</sub>S and (b) a-Li<sub>x</sub>Si, respectively. (a) The blue diamond symbols denote the calculated  $J_{IC}$ . A variety of integral domains with inner radii as 50 and 60 Å and outer radii as 90, 100, 110 and 120 Å are calculated, with the error bars indicating the standard deviation from statistical analyses across eight different integral domains for every a-Li<sub>x</sub>S. The red star symbolizes results from our MD simulations with stress-strain curves available in Fig. S6, while red circles represent results from Ref. (Islam et al., 2015), which are consistent with our results. (b) The blue triangle and sphere points correspond to the fracture energy of a-Li<sub>x</sub>Si obtained by experiments and MD simulations, respectively (Wang et al., 2015; Yang and Qu, 2019). The red points correspond to yield strength under uniaxial tension by experiments, DFT, ReaxFF-based MD and MEAM based MD simulations, respectively (Khosrownejad and Curtin, 2017; Sethuraman et al., 2010; Wang and Chew, 2016).

lithium incorporation into different atomic structures. We have provided comprehensive rationale for our atomistic observations. Last, we remain committed to pursuing direct experimental validations of our findings.

#### 4. Conclusion

In summary, through large-scale atomistic simulations, we have uncovered the atomic-scale fracture mechanisms in a-LixS across varying lithium concentrations. Results indicate that at lower lithium concentrations, brittle fracture occurs due to nucleation and coalescence of nanoscale cavities ahead of the crack tip. While at higher lithium concentrations, the cavitation phenomenon is suppressed, and plastic deformation is regulated by extensive shear bands, resulting in more ductile fracture behavior. The transition between these fracture mechanisms is determined by whether the local hydrostatic stress at the crack tip exceeds the critical cavitation stress. At the atomic level, local chemical bonding dynamics shift from isolated bond ruptures to a more generalized bond reformation. The atomic chain bridging is simultaneously presented behind the crack tip to enhance crack resistance at lower lithium concentrations. Furthermore, we conduct domain J-integral analysis and uniaxial tensile loading tests to ascertain fracture energy and strength at different lithium concentrations, thereby quantifying a previously unobserved strength-ductility synergy induced by electrochemical process of lithiation into ring structured sulfur. These insights shed light on the fracture tendencies of sulfur cathodes in lithium-ion batteries and pave the way for designing robust cathodes in the future. Last, the chemical modulation as lithiation in this study represents a more intuitive approach for achieving strength-ductility synergy, potentially inspiring further research in this field.

#### CRediT authorship contribution statement

**Yuan Gao:** Investigation, Methodology, Visualization, Writing – original draft. **Siyi Huang:** Methodology. **Xiaoyan Li:** Supervision, Validation. **Yuli Chen:** Funding acquisition, Supervision, Validation. **Bin Ding:** Conceptualization, Supervision, Validation, Funding acquisition, Writing – original draft, Writing – review & editing.

#### Declaration of competing interest

The authors declare that they have no known competing financial interests or personal relationships that could have appeared to influence the work reported in this paper.

#### Data availability

Data will be made available on request.

#### Acknowledgements

This work was financially support by the National Natural Science Foundation of China (Grant Nos.12102021, 12372105 and 12172026) and the Fundamental Research Funds for the Central Universities. The work was carried out at National Supercomputer Center in Tianjin, and the calculations were performed on TianHe-1(A).

#### Supplementary materials

Supplementary material associated with this article can be found, in the online version, at [doi:10.1016/j.ijplas.2024.103891](https://doi.org/10.1016/j.ijplas.2024.103891).

#### Appendix A. Supporting information

Supplementary data associated with this article can be found, in the online version, at [doi:10.1016/j.ijplas.2024.103891](https://doi.org/10.1016/j.ijplas.2024.103891).

#### References

- Bai, Y., Nguyen, T.T., Chu, R., Kim, N.H., Lee, J.H., 2023. Core-shell hollow nanostructures as highly efficient polysulfide conversion and adsorption cathode for shuttle-free lithium-sulfur batteries. *Chem. Eng. J.* 454, 140338. <https://doi.org/10.1016/j.cej.2022.140338>.
- Chan, C.K., Peng, H., Liu, G., McIlwraith, K., Zhang, X.F., Huggins, R.A., Cui, Y., 2008. High-performance lithium battery anodes using silicon nanowires. *Nat. Nanotechnol.* 3, 31–35. <https://doi.org/10.1038/nano.2007.411>.
- Chen, L., Dietz Rago, N.L., Bloom, I.D., Shaw, L.L., 2016. New insights into the electrode mechanism of lithium sulfur batteries via air-free post-test analysis. *Chem. Commun.* 52, 9913–9916. <https://doi.org/10.1039/c6cc04401h>.
- Chen, R., Zhou, Y., Li, X., 2022a. Cotton-derived Fe/Fe3C-encapsulated carbon nanotubes for high-performance lithium–sulfur batteries. *Nano Lett.* 22, 1217–1224. <https://doi.org/10.1021/acs.nanolett.1c04380>.
- Chen, S., Aitken, Z.H., Pattamatta, S., Wu, Z., Yu, Z.G., Srolovitz, D.J., Liaw, P.K., Zhang, Y.-W., 2021. Simultaneously enhancing the ultimate strength and ductility of high-entropy alloys via short-range ordering. *Nat. Commun.* 12, 4953. <https://doi.org/10.1038/s41467-021-25264-5>.

- Chen, W., He, W., Jiang, B., Pan, F., 2022b. Simultaneous enhancement of strength and ductility for AZ31 magnesium alloy by pre-twinning induced heterostructure. *Int. J. Plast.* 159, 103483 <https://doi.org/10.1016/j.ijplas.2022.103483>.
- de Vasconcelos, L.S., Xu, R., Xu, Z., Zhang, J., Sharma, N., Shah, S.R., Han, J., He, X., Wu, X., Sun, H., 2022. Chemomechanics of rechargeable batteries: status, theories, and perspectives. *Chem. Rev.* 122, 13043–13107. <https://doi.org/10.1021/acs.chemrev.2c00002>.
- Ding, B., Li, X., Zhang, X., Wu, H., Xu, Z., Gao, H., 2015. Brittle versus ductile fracture mechanism transition in amorphous lithiated silicon: from intrinsic nanoscale cavitation to shear banding. *Nano Energy* 18, 89–96. <https://doi.org/10.1016/j.nanoen.2015.10.002>.
- Ding, B., Wu, H., Xu, Z., Li, X., Gao, H., 2017. Stress effects on lithiation in silicon. *Nano Energy* 38, 486–493. <https://doi.org/10.1016/j.nanoen.2017.06.021>.
- Ghaemi, M., Jafary-Zadeh, M., Khoo, K.H., Gao, H., 2022. Chemical affinity can govern notch-tip brittle-to-ductile transition in metallic glasses. *Extreme Mech. Lett.* 52, 101651 <https://doi.org/10.1016/j.eml.2022.101651>.
- Hasan, M., Liu, Y., An, X., Gu, J., Song, M., Cao, Y., Li, Y., Zhu, Y., Liao, X., 2019. Simultaneously enhancing strength and ductility of a high-entropy alloy via gradient hierarchical microstructures. *Int. J. Plast.* 123, 178–195. <https://doi.org/10.1016/j.ijplas.2019.07.017>.
- He, M., Shen, Y., Jia, N., Liaw, P., 2021. C and N doping in high-entropy alloys: a pathway to achieve desired strength-ductility synergy. *Appl. Mater. Today* 25, 101162. <https://doi.org/10.1016/j.apmt.2021.101162>.
- Holeki Chandrappa, M.L., Qi, J., Chen, C., Banerjee, S., Ong, S.P., 2022. Thermodynamics and kinetics of the cathode-electrolyte interface in all-solid-state Li–S batteries. *J. Am. Chem. Soc.* 144, 18009–18022. <https://doi.org/10.1021/jacs.2c07482>.
- Islam, M.M., Ostadhossien, A., Borodin, O., Yeates, A.T., Tipton, W.W., Hennig, R.G., Kumar, N., van Duin, A.C., 2015. ReaxFF molecular dynamics simulations on lithiated sulfur cathode materials. *Phys. Chem. Chem. Phys.* 17, 3383–3393. <https://doi.org/10.1039/c4cp04532g>.
- Jones, R.E., Zimmerman, J.A., 2010. The construction and application of an atomistic J-integral via Hardy estimates of continuum fields. *J. Mech. Phys. Solids* 58, 1318–1337. <https://doi.org/10.1016/j.jmps.2010.06.001>.
- Khosronejad, S.M., Curtin, W.A., 2017. Crack growth and fracture toughness of amorphous Li–Si anodes: mechanisms and role of charging/discharging studied by atomistic simulations. *J. Mech. Phys. Solids* 107, 542–559. <https://doi.org/10.1016/j.jmps.2017.06.010>.
- Khosronejad, S.M., Kermode, J.R., Pastewka, L., 2021. Quantitative prediction of the fracture toughness of amorphous carbon from atomic-scale simulations. *Phys. Rev. Mater.* 5, 023602 <https://doi.org/10.1103/PhysRevMaterials.5.023602>.
- Kim, R.E., Kim, E.S., Karthik, G.M., Gu, G.H., Ahn, S.Y., Park, H., Moon, J., Kim, H.S., 2022. Heterostructured alloys with enhanced strength-ductility synergy through laser-cladding. *Scri. Mater.* 215, 114732 <https://doi.org/10.1016/j.scriptamat.2022.114732>.
- Kim, T., Song, W., Son, D.-Y., Ono, I.K., Qi, Y., 2019. Lithium-ion batteries: outlook on present, future, and hybridized technologies. *J. Mater. Chem. A* 7, 2942–2964. <https://doi.org/10.1039/C8TA10513H>.
- Lee, B.-J., Zhao, C., Yu, J.-H., Kang, T.-H., Park, H.-Y., Kang, J., Jung, Y., Liu, X., Li, T., Xu, W., 2022. Development of high-energy non-aqueous lithium-sulfur batteries via redox-active interlayer strategy. *Nat. Commun.* 13, 4629. <https://doi.org/10.1038/s41467-022-31943-8>.
- Li, X., Gao, H., 2015. Atomistic modelling of deformation and failure mechanisms in nanostructured materials. *Natl. Sci. Rev.* 2, 133–136. <https://doi.org/10.1093/nsr/nwu049>.
- Li, Y., Zhang, J., Zhang, K., Zheng, B., Yang, F., 2019. A defect-based viscoplastic model for large-deformed thin film electrode of lithium-ion battery. *Int. J. Plast.* 115, 293–306. <https://doi.org/10.1016/j.ijplas.2018.12.001>.
- Liu, J., Zhong, Y., Mu, K., Han, T., Zhang, H., Si, T., 2021. A self-healing lithium–sulfur battery using gel-infilled microcapsules. *ACS Appl. Energy Mater.* 4, 6749–6756. <https://doi.org/10.1021/acsaem.c00857>.
- Liu, X., Huang, J.Q., Zhang, Q., Mai, L., 2017. Nanostructured metal oxides and sulfides for lithium–sulfur batteries. *Adv. Mater.* 29, 1601759 <https://doi.org/10.1002/adma.201601759>.
- Luo, C., Hu, E., Gaskell, K.J., Fan, X., Gao, T., Cui, C., Ghose, S., Yang, X.-Q., Wang, C., 2020a. A chemically stabilized sulfur cathode for lean electrolyte lithium sulfur batteries. *Proc. Natl. Acad. Sci.* 117, 14712–14720. <https://doi.org/10.1073/pnas.2006301117>.
- Luo, X., Feng, Z., Yu, T., Luo, J., Huang, T., Wu, G., Hansen, N., Huang, X., 2020b. Transitions in mechanical behavior and in deformation mechanisms enhance the strength and ductility of Mg–3Gd. *Acta Mater.* 183, 398–407. <https://doi.org/10.1016/j.actamat.2019.11.034>.
- Manthiram, A., Fu, Y., Chung, S.-H., Zu, C., Su, Y.-S., 2014. Rechargeable lithium–sulfur batteries. *Chem. Rev.* 114, 11751–11787. <https://doi.org/10.1021/cr500062v>.
- Manthiram, A., Fu, Y., Su, Y.-S., 2013. Challenges and prospects of lithium–sulfur batteries. *Acc. Chem. Res.* 46, 1125–1134. <https://doi.org/10.1021/ar300179v>.
- Mayer, A.E., Mayer, P.N., 2019. Evolution of pore ensemble in solid and molten aluminum under dynamic tensile fracture: molecular dynamics simulations and mechanical models. *Int. J. Mech. Sci.* 157, 816–832. <https://doi.org/10.1016/j.ijmecsci.2019.05.023>.
- Monismith, S., Qu, J., Dingreville, R., 2022. Grain-boundary fracture mechanisms in Li<sub>7</sub>La<sub>3</sub>Zr<sub>2</sub>O<sub>12</sub> (LLZO) solid electrolytes: when phase transformation acts as a temperature-dependent toughening mechanism. *J. Mech. Phys. Solids* 160, 104791. <https://doi.org/10.1016/j.jmps.2022.104791>.
- Murali, P., Guo, T., Zhang, Y., Narasimhan, R., Li, Y., Gao, H., 2011. Atomic scale fluctuations govern brittle fracture and cavitation behavior in metallic glasses. *Phys. Rev. Lett.* 107, 215501 <https://doi.org/10.1103/PhysRevLett.107.215501>.
- Plimpton, S., 1995. Fast parallel algorithms for short-range molecular dynamics. *J. Comput. Phys.* 117, 1–19. <https://doi.org/10.1006/jcph.1995.1039>.
- Pogorelko, V.V., Mayer, A.E., 2023. Dynamic tensile fracture of iron: molecular dynamics simulations and micromechanical model based on dislocation plasticity. *Int. J. Plast.* 03678. <https://doi.org/10.1016/j.ijplas.2023.103678>.
- Rice, J.R., 1968. A path independent integral and the approximate analysis of strain concentration by notches and cracks. *J. Appl. Mech.* 35, 379–386. <https://doi.org/10.1115/1.3601206>.
- Sandu, G., Brassart, L., Gohy, J.-F., Pardoen, T., Melinte, S., Vlad, A., 2014. Surface coating mediated swelling and fracture of silicon nanowires during lithiation. *ACS Nano* 8, 9427–9436. <https://doi.org/10.1021/nn503564r>.
- Senftle, T.P., Hong, S., Islam, M.M., Kylasa, S.B., Zheng, Y., Shin, Y.K., Junkermeier, C., Engel-Herbert, R., Janik, M.J., Aktulga, H.M., Verstraelen, T., Grama, A., van Duin, A.C.T., 2016. The ReaxFF reactive force-field: development, applications and future directions. *npj Comput. Mater.* 2 <https://doi.org/10.1038/npjcomputmat.2015.11>.
- Sethuraman, V.A., Chon, M.J., Shimshak, M., Srinivasan, V., Guduru, P.R., 2010. In situ measurements of stress evolution in silicon thin films during electrochemical lithiation and delithiation. *J. Power Sources* 195, 5062–5066. <https://doi.org/10.1016/j.jpowsour.2010.02.013>.
- Shao, Q., Zhu, S., Chen, J., 2023. A review on lithium–sulfur batteries: challenge, development, and perspective. *Nano Res.* 1–42. <https://doi.org/10.1007/s12274-022-5227-0>.
- Shen, L., Yu, J., Tang, X., Sun, B., Liu, Y., Bai, H., Wang, W., 2021. Observation of cavitation governing fracture in glasses. *Sci. Adv.* 7, eabf7293. <https://doi.org/10.1126/sciadv.abf7293>.
- Singh, A., Pal, S., 2020. Coupled chemo-mechanical modeling of fracture in polycrystalline cathode for lithium-ion battery. *Int. J. Plast.* 127, 102636 <https://doi.org/10.1016/j.ijplas.2019.11.015>.
- Tancogne-Dejean, T., Gorji, M.B., Zhu, J., Mohr, D., 2021. Recurrent neural network modeling of the large deformation of lithium-ion battery cells. *Int. J. Plast.* 146, 103072 <https://doi.org/10.1016/j.ijplas.2021.103072>.
- Wang, H., Chew, H.B., 2016. Molecular dynamics simulations of plasticity and cracking in lithiated silicon electrodes. *Extreme Mech. Lett.* 9, 503–513. <https://doi.org/10.1016/j.eml.2016.02.020>.
- Wang, M., Yu, J., Lin, S., 2017. Lithiation-assisted strengthening effect and reactive flow in bulk and nanoconfined sulfur cathodes of lithium–sulfur batteries. *J. Phys. Chem. C* 121, 17029–17037. <https://doi.org/10.1021/acs.jpcc.7b05446>.
- Wang, X., Fan, F., Wang, J., Wang, H., Tao, S., Yang, A., Liu, Y., Beng Chew, H., Mao, S.X., Zhu, T., Xia, S., 2015. High damage tolerance of electrochemically lithiated silicon. *Nat. Commun.* 6, 8417. <https://doi.org/10.1038/ncomms9417>.
- Wang, Z., Li, Y., Ji, H., Zhou, J., Qian, T., Yan, C., 2022. Unity of opposites between soluble and insoluble lithium polysulfides in lithium–sulfur batteries. *Adv. Mater.* 34, 2203699 <https://doi.org/10.1002/adma.202203699>.

- Xiang, H., Guo, W., 2022. Synergistic effects of twin boundary and phase boundary for enhancing ultimate strength and ductility of lamellar TiAl single crystals. *Int. J. Plast.* 150, 103197 <https://doi.org/10.1016/j.ijplas.2021.103197>.
- Xie, W., Zhang, X., Wei, Y., Gao, H., 2023. Toughening two dimensional materials through lattice disorder. *Carbon*, 118268. <https://doi.org/10.1016/j.carbon.2023.118268>.
- Yang, H., Qu, J., 2019. Fracture toughness of Li<sub>x</sub>Si alloys in lithium ion battery. *Extreme Mech. Lett.* 32, 100555 <https://doi.org/10.1016/j.eml.2019.100555>.
- Yang, X., Luo, J., Sun, X., 2020. Towards high-performance solid-state Li–S batteries: from fundamental understanding to engineering design. *Chem. Soc. Rev.* 49, 2140–2195. <https://doi.org/10.1039/c9cs00635d>.
- Zeng, Y., Zhang, Q., Wang, Y., Jiang, J., Xing, H., Li, X., 2021. Toughening and crack healing mechanisms in nanotwinned diamond composites with various polytypes. *Phys. Rev. Lett.* 127, 066101 <https://doi.org/10.1103/PhysRevLett.127.066101>.
- Zhang, Y., Luo, Y., Fincher, C., McProuty, S., Swenson, G., Banerjee, S., Pharr, M., 2019. In-situ measurements of stress evolution in composite sulfur cathodes. *Energy Storage Mater.* 16, 491–497. <https://doi.org/10.1016/j.ensm.2018.10.001>.
- Zhu, J., Li, W., Wierzbicki, T., Xia, Y., Harding, J., 2019. Deformation and failure of lithium-ion batteries treated as a discrete layered structure. *Int. J. Plast.* 121, 293–311. <https://doi.org/10.1016/j.ijplas.2019.06.011>.